Research on Influence of Low Coupling Capacitance in the RENA-3-Based Particle Detection System

YANG Xin[1,2], *WANG Linghua*[1,2*], *YU Xiangqian*[1,2], *SHI Weihong*[1], *CHEN Hongfei*[1], *WANG Youlong*[1], *WANG Yongfu*[1], *ZONG Qiugang*[1], *ZOU Hong*[1], *YE Yuguang*[1]

1. Institute of Space Physics and Applied Technology, School of Earth and Space Sciences, Peking University, Beijing 100871, P. R. China; 2. State Key Laboratory of Solar Activity and Space Weather, National Space Science Center, Chinese Academy of Sciences, Beijing 100190, P. R. China

(Received 19 July 2025; revised 11 January 2026; accepted 8 April 2026)

Abstract: The performance of a particle detection system is primarily determined by its first stage, which mainly includes a particle radiation detector and a charge-sensitive preamplifier (CSA). The connection between the detector and the front-end readout circuit is typically AC-coupled, which usually has a coupling capacitor in the range of 0.01—0.1 μF to isolate the input of the CSA from the detector. The application-specific integrated circuit (ASIC) readout electronics for nuclear applications 3(RENA-3) is a multi-channel mixed-signal integrated circuit (IC) offering high energy resolution and high time resolution, developed for the readout of particle radiation detectors. RENA-3 is employed as the front-end readout circuit for an interplanetary energetic particle telescope designed to detect 20—1 000 keV electrons, 25—12 000 keV protons, and ions like alpha particles. However, the maximum input charge of RENA-3 is 54 fC, which limits its maximum detection range to about 1 200 keV and is insufficient for the proton channels. While other ASICs could be adopted, available alternatives do not simultaneously meet the requirements for both high precision and wide measurement range. This paper proposes the use of a small coupling capacitance to extend the range for proton detection by attenuating the charge signal before it reaches the CSA input. The coupling capacitance is on the order of picofarads, much smaller than the detector junction capacitance. In this configuration, stray capacitance and coupling capacitance become significant. A circuit theoretical model is proposed to calculate the transfer function from input charge to output voltage, analyzing the influence of coupling capacitance and stray capacitance on the particle radiation detection system. Experiments using discrete components with known parameters are conducted to validate the theoretical model. Finally, the model is applied to the RENA-3 system for optimization to meet the instrument's specifications, and certain RENA-3 parameters are derived.

Key words: AC-coupled circuit; coupling capacitance; stray capacitance; circuit performance; particle radiation detection system

CLC number: TN722 **Document code:** A **Article ID:** 1005-1120(2026)04-0506-11

0 Introduction

The performance of a particle detection system is primarily determined by its first stage, which mainly includes a detector and a charge-sensitive preamplifier (CSA)[1-2]. To improve system performance, it is crucial to maximize the output signal amplitude and minimize noise at the first stage[3-4]. In addition to the quality of the detector and CSA, the system performance is also affected by their interconnection[5-7]. The coupling between the detector and CSA is always AC-coupled, which usually has a coupling capacitor of 0.01—0.1 μF to isolate the input of the CSA from the detector[8-9]. Stray ca-

*Corresponding author, E-mail address: wanglhwang@pku.edu.cn.

How to cite this article: YANG Xin, WANG Linghua, YU Xiangqian, et al. Research on influence of low coupling capacitance in the RENA-3-based particle detection system[J]. Transactions of Nanjing University of Aeronautics and Astronautics, 2026, 43(4): 506-516.

http://dx.doi.org/10.16356/j.1005-1120.2026.04.002

pacitance between the detector and CSA is also inevitable. Both coupling and stray capacitances can affect the detection performance. In conventional AC-coupled circuits, the coupling capacitance is usually much larger than the detector junction capacitance and stray capacitance (The latter is typically on the order of picofarads). Therefore, the detector junction capacitance and stray capacitance are often neglected.

The deep space exploration in China is still in its infancy. In order to achieve specific scientific goals, we need to develop instruments with higher precision and better performance[10]. The interplanetary ultralow-noise three-dimensional energetic particle spectrometer (IEPS) is designed to detect 20—1 000 keV electrons, 25—12 000 keV protons, and ions like alpha particles, with the detector capacitance ranging from tens to hundreds of picofarads. The IEPS is a double-ended particle spectrometer with a four-layer semiconductor detector: One end is designed for electron detection and the other for protons and heavy ions[11]. To achieve low-noise, high-precision detection, the readout electronics for nuclear applications 3 (RENA-3) [12] is selected as the ASIC. RENA-3 is a multi-channel, high-energy-resolution, high-time-resolution mixed-signal integrated circuit (IC) developed for the particle radiation detector readout. It has been successfully used as an integrated preamplifier ASIC in numerous particle spectrometers[13-16]. However, the maximum input charge of RENA-3 is 54 fC, with a linear range experimentally around 100 fC, limiting its detectable energy to about 1 200 keV (2 200 keV in experiments). While it meets the energy range requirement for electron channels with high resolution, it is insufficient for proton and heavy ion channels. Simulations indicate that the energy range of RENA-3 needs to be extended by at least a factor of four for the first layer detector to enable alpha particle detection. Alternatively, other ASICs could be adopted. However, high-precision electron detection is critical for our project, and available ASICs do not simultaneously satisfy both high precision and wide measurement range requirements. For instance, the lowest noise levels of VATA462 (325 e^-, where e^- is one electron) and IDE3466 (<0.13 fC $\approx$ 800 e^-) are higher than that of RENA-3 (<280 e^-). Reducing the coupling capacitance to a value on the order of picofarads, much smaller than the detector junction capacitance, can attenuate the charge entering the CSA, offering a potential method to extend the energy range for proton channels. In this case, stray capacitance and coupling capacitance cannot be ignored and will significantly influence the circuit performance. This paper proposes a circuit theoretical model to calculate the transfer function from input charge to output voltage, analyzing the influence of coupling capacitance, detector junction capacitance, and stray capacitance on the particle radiation detection system.

1 Theoretical Background

A typical circuit schematic of the AC-coupled connection between the detector and CSA is shown in Fig.1[6, 8-9]. As illustrated, the DC bias supply V_{bias} feeds the detector through a bias resistor R_{b}, and the coupling capacitor C_x isolates the CSA input from the detector. This allows V_{bias} to be adjusted without affecting the CSA, enabling the use of different R_{b} values without altering the CSA input. C_{d} denotes the detector junction capacitance. C_{s1} denotes the stray capacitance between the detector and coupling capacitor while C_{s2} denotes the stray capacitance between the coupling capacitor and CSA. The values of C_{s1} and C_{s2} depend on the wiring layout. C_x blocks DC current from the detector, making it suitable for detectors with high leakage current. The charge signal generated by the detector reaches the CSA via C_x. The coupling capacitance should match the input impedance of the preamplifier.

As shown in Fig.1, the detector generates a current pulse with charge Q, proportional to the energy

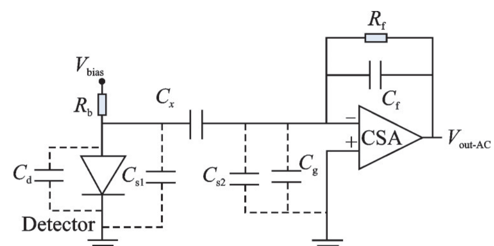

Fig.1 Circuit schematic of the AC-coupled arrangement between detector and preamplifier

deposited by particles in the detector. Assuming the preamplifier has ideal impedance (infinite input impedance and zero output impedance) and the charge collection time is much shorter than the rise time of the amplifier, then the CSA output amplitude is

$$V_{\text{out-CSA}}=Q\left\{\frac{1+A}{(1+A)C_{\mathrm{f}}+C_{\mathrm{g}}+C_{\mathrm{s2}}}\right\}\times\frac{C_{\mathrm{in1}}}{C_{\mathrm{in1}}+C_{\mathrm{s1}}+C_{\mathrm{d}}}\tag{1}$$

where A is the open-loop gain of the preamplifier (typically 10^5—$10^6\gg 1$); C_{f} indicates the feedback capacitor of CSA; C_{g} corresponds to the input capacitor of CSA; C_{in1} corresponds to the equivalent capacitance from the detector terminal to the CSA.

$$C_{\mathrm{in1}}=\frac{C_{\mathrm{g}}+C_{\mathrm{s2}}+(1+A)C_{\mathrm{f}}}{C_x+C_{\mathrm{g}}+C_{\mathrm{s2}}+(1+A)C_{\mathrm{f}}}C_x\tag{2}$$

The CSA output passes through a capacitor-resistor-resistor-capacitor (CR-RC) shaping network to form a Gaussian signal. The shaping network has a linear transfer function with a fixed coefficient A_2 for a given particle detection system. A_2 may vary with frequency, but in the experiments of the following sections the input frequency is constant, so A_2 is treated as fixed. The output amplitude after shaping is

$$V_{\text{out-shape}}=A_2Q\left\{\frac{1+A}{(1+A)C_{\mathrm{f}}+C_{\mathrm{g}}+C_{\mathrm{s2}}}\right\}\times\frac{C_{\mathrm{in1}}}{C_{\mathrm{in1}}+C_{\mathrm{s1}}+C_{\mathrm{d}}}\tag{3}$$

In addition to the amplitude of the output voltage, the noise is also important. The noise model is shown in Fig.2, with main sources as follows.

(1) $2i_{\mathrm{d}}q\mathrm{d}f$ ($\mathrm{d}\,\overline{i^2_{i_{\mathrm{d}}}}$) is the detector shot noise, which is caused by the detector leakage current i_{d}.

(2) $4kT/R_{\mathrm{b}}\mathrm{d}f$ ($\mathrm{d}\,\overline{i^2_{R_{\mathrm{b}}}}$) is bias resistor thermal noise which is caused by R_{b}.

(3) $2i_{\mathrm{g}}q\mathrm{d}f$ ($\mathrm{d}\,\overline{i^2_{i_{\mathrm{g}}}}$) is junction field-effect transistor (JFET) shot noise which is caused by the gate leakage current i_{g} and it constitutes the main noise of JFET.

(4) $4kT/R_{\mathrm{f}}\mathrm{d}f$ ($\mathrm{d}\,\overline{i^2_{R_{\mathrm{f}}}}$) is feedback resistor thermal noise which is caused by R_{f}.

(5) $K_{\mathrm{F}}/(C_{\mathrm{g}}f)\mathrm{d}f$ ($\mathrm{d}\,\overline{v^2_{\mathrm{f}}}$) is JFET flicker noise.

(6) $8kT/(3g_{\mathrm{m}})\mathrm{d}f$ ($\mathrm{d}\,\overline{v^2_{c_{\mathrm{h}}}}$) is JFET thermal noise.

(7) $4kT/(g_{\mathrm{m}}^2R_{\mathrm{d}})\mathrm{d}f$ ($\mathrm{d}\,\overline{v^2_{R_{\mathrm{d}}}}$) is drain resistor thermal noise.

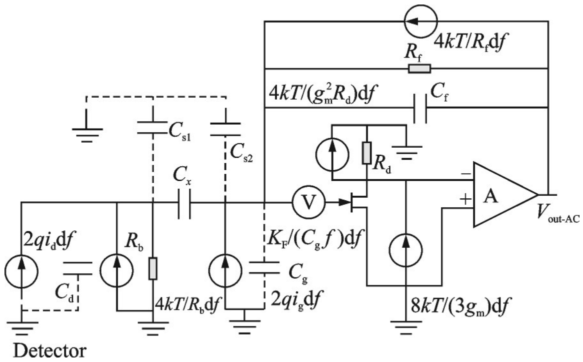

Fig.2 Noise model of AC-coupled arrangement

Finally, all noise sources are mapped to the output of the preamplifier. $\overline{i^2_{i_{\mathrm{d}}}}$, $\mathrm{d}\,\overline{i^2_{R_{\mathrm{b}}}}$, $\mathrm{d}\,\overline{i^2_{i_{\mathrm{g}}}}$, and $\mathrm{d}\,\overline{i^2_{R_{\mathrm{f}}}}$ are current noises located at the preamplifier input[6]. For an ideal amplifier, current noise at the input flows through C_{f} to the output, giving the relationship: $V^2_{\text{noise}}=\mathrm{d}i^2/(\omega C_{\mathrm{f}})^2$. Summing these contributions yields the squared output noise voltage due to current noise: $(2i_{\mathrm{d}}q+4kT/R_{\mathrm{b}}+2i_{\mathrm{g}}q+4kT/R_{\mathrm{f}})/(\omega C_{\mathrm{f}})^2\mathrm{d}f$, where ω denotes the radian frequency, and the value is equal to $2\pi f$. Voltage noise sources $\mathrm{d}\,\overline{v^2_{\mathrm{f}}}$, $\mathrm{d}\,\overline{v^2_{c_{\mathrm{h}}}}$, and $\mathrm{d}\,\overline{v^2_{R_{\mathrm{d}}}}$ are also referred to the preamplifier input[6]. For an ideal amplifier, the output noise voltage due to voltage noise is amplified by the factor: $(1+C_{\mathrm{in}}/C_{\mathrm{f}})$. Here, C_{in} is the capacitance looking back from the gate toward the detector: $C_{\mathrm{in}}=C_{\mathrm{g}}+C_{\mathrm{s2}}+C_x(C_{\mathrm{d}}+C_{\mathrm{s1}})/(C_x+C_{\mathrm{d}}+C_{\mathrm{s1}})$. Thus, the squared output noise voltage from voltage noise is $(K_{\mathrm{F}}/(C_{\mathrm{g}}f)+8kT/(3g_{\mathrm{m}})+4kT/(R_{\mathrm{d}}g_{\mathrm{m}}^2))\times(1+C_{\mathrm{in}}/C_{\mathrm{f}})^2\mathrm{d}f$. Although C_x does not introduce additional noise, it alters the noise coupling, thereby affecting the output noise. The total output noise voltage of the CSA is

$$\overline{v^2_{\text{noise-CSA}}}=\left(2i_{\mathrm{d}}q+\frac{4kT}{R_{\mathrm{b}}}+2i_{\mathrm{g}}q+\frac{4kT}{R_{\mathrm{f}}}\right)\Big/(\omega C_{\mathrm{f}})^2\mathrm{d}f+\left(\frac{K_{\mathrm{F}}}{C_{\mathrm{g}}f}+\frac{8kT}{3g_{\mathrm{m}}}+\frac{4kT}{R_{\mathrm{d}}g_{\mathrm{m}}^2}\right)\left(1+\frac{C_{\mathrm{g}}+C_{\mathrm{s2}}}{C_{\mathrm{f}}}+\frac{C_x(C_{\mathrm{d}}+C_{\mathrm{s1}})}{C_{\mathrm{f}}(C_{\mathrm{d}}+C_{\mathrm{s1}}+C_x)}\right)^2\mathrm{d}f\tag{4}$$

The signal from the CSA passes through a CR-RC shaping network to form a Gaussian signal. The transfer function is $A(\omega)=A_0\omega\tau/(1+\omega^2\tau^2)$[6], where A_0 denotes a constant relative to the gain of the network, $\omega=2\pi f$ corresponds to the frequency, and τ is the time constant of the CR or RC network, which is also called the shaping time constant.

Therefore, the output noise of the shaping network is given by

$$\overline{v^2_{\text{noise-shape}}}=\int_0^\infty |A(\omega)|^2\,\overline{v^2_{\text{noise-CSA}}}=$$
$$\frac{\tau A_0^2}{C_f^2}\left(\frac{kT}{2R_b}+\frac{kT}{2R_f}+\frac{qi_d}{4}+\frac{qi_g}{4}\right)+$$
$$\left(\frac{K_f A_0^2}{2C_g}+\frac{kTA_0^2}{3\tau g_m}+\frac{kTA_0^2}{2\tau R_d g_m^2}\right)$$
$$\left(1+\frac{C_g+C_{s2}}{C_f}+\frac{1}{C_f}\left(\frac{(C_d+C_{s1})C_x}{C_d+C_{s1}+C_x}\right)\right)^2 \tag{5}$$

The equivalent noise charge (ENC) for a CR-RC shaping network can be calculated by

$$\mathrm{ENC}_{\text{noise}}=\frac{eC_f}{A_0}\sqrt{\overline{v^2_{\text{noise-shape}}}} \tag{6}$$

where $e\approx 1.602\times10^{-19}$ C is the elementary charge.

2 Experiment Validation

Since some key parameters of RENA-3 are unavailable, experiments using discrete components with known parameters are conducted to validate the theoretical models. The applicability of these models to the RENA-3 system will be verified in the next section. Three experiments are performed, each varying only one capacitance (coupling capacitance C_x, stray capacitance C_{s1} or stray capacitance C_{s2}) while keeping other electronics constant.

Fig.3 shows the block diagram of the experiment. To conveniently vary the equivalent detector junction capacitance, an equivalent output charge method (inside the dotted frame) is used to simulate the process of particles entering the detector and generating charges. C_d represents the equivalent detector capacitance and R_d the equivalent detector resistance. A voltage signal with 80 ns rise time, 400 μs fall time, and amplitude V is used to generate an equivalent charge. The equivalent input charge $Q_{in}=V\times C_{input}$, where C_{input} is 1 pF. We set V between 10 mV to 200 mV and make sure $V_{\text{out-CSA}}$ being always kept below 54 fC. C_x is coupling capacitance which can be changed by replacing the capacitor. C_{s1} and C_{s2} represent stray capacitance as defined earlier. A 3DJ8I JFET is used as the first-stage input, and a TL082M op-amp is served as the CSA amplifier. After the main amplifier, we read out the data using ORTEC's multichannel analyzer. Specific experimental parameters are listed in Table 1, and results are normalized to the max value.

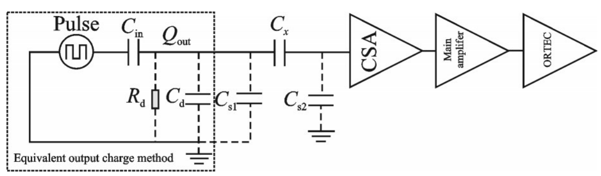

Fig.3 Block diagram of discrete component experiments

Table 1 Parameters for calculation

Parameter	Value	Parameter	Value	Parameter	Value
i_g/A	10×10^{-9}	k(Boltzmann constant)/(J•K^{-1})	$1.380\,649\times10^{-23}$	R_f/MΩ	100
C_g/pF	8	T/K	300(27 ℃)	C_f/pF	3
g_m/mS	15	A	730	R_b/MΩ	100
K_F/J	5×10^{-28}	R_d/kΩ	6.1	τ/μs	1.1

Figs.4 and 5 show the normalized output signal amplitude and noise of the shaping network ($V_{\text{out-shape}}$) versus coupling capacitance C_x, with other parameters fixed. Data points marked "○" are experimental results and the solid line is theoretical result. The same convention applies to Figs. 4—12. As shown, both output amplitude and noise increase with C_x. Experimental results agree with theoretical analysis, confirming that the energy range can be extended by selecting an appropriate coupling capacitor.

Based on the above experiments with coupling capacitance, when the energy range is expanded by approximately a factor of four, experimental results

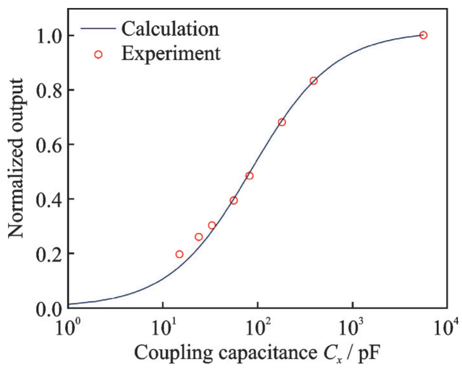

Fig.4 Relationship between the output signal amplitude of the shaping network $V_{\text{out-shape}}$ and coupling capacitance C_x

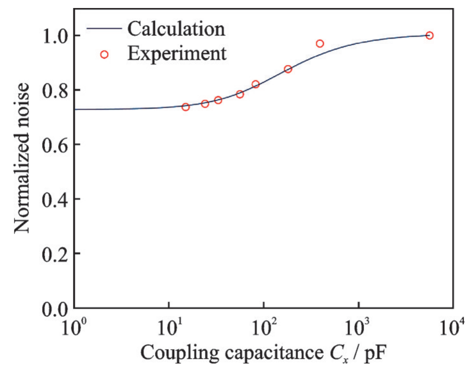

Fig.5 Relationship between the output noise of the shaping network $V_{\text{out-shape}}$ and coupling capacitance C_x

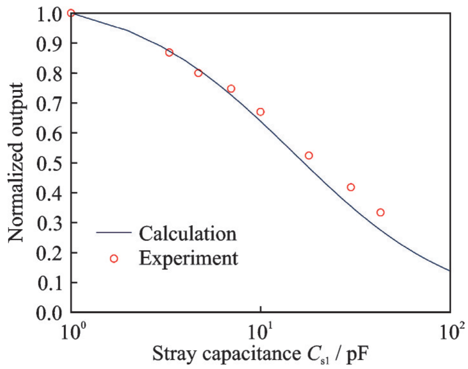

Fig.6 Relationship between the output signal amplitude of the shaping network $V_{\text{out-shape}}$ and C_{s1}

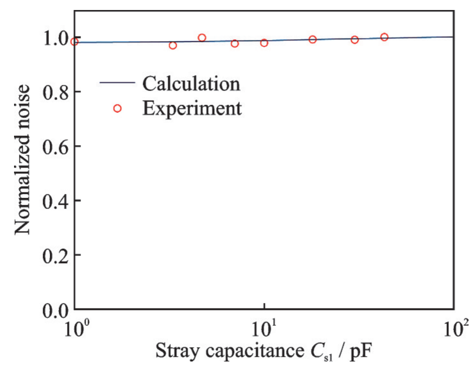

Fig.7 Relationship between the output signal noise of the shaping network $V_{\text{out-shape}}$ and C_{s1}

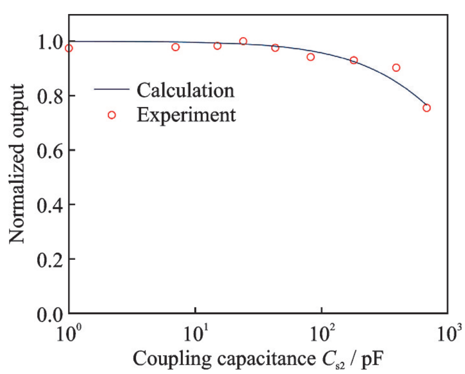

Fig.8 Relationship between the output signal amplitude of the shaping network $V_{\text{out-shape}}$ and C_{s2}

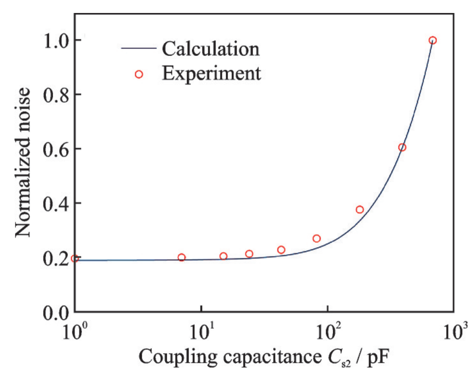

Fig.9 Relationship between the output signal noise of the shaping network $V_{\text{out-shape}}$ and C_{s2}

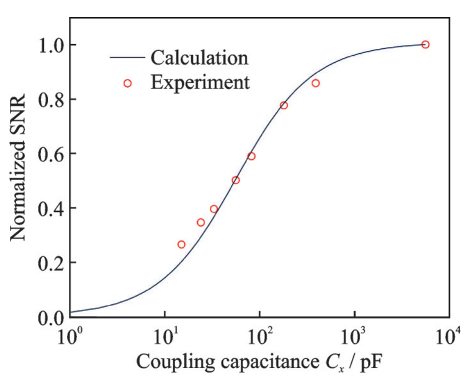

Fig.10 Relationship between SNR and coupling capacitance C_x

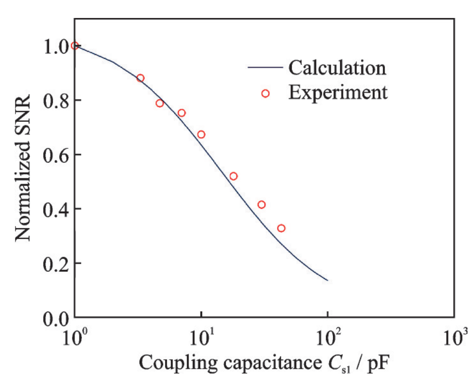

Fig.11 Relationship between SNR and C_{s1}

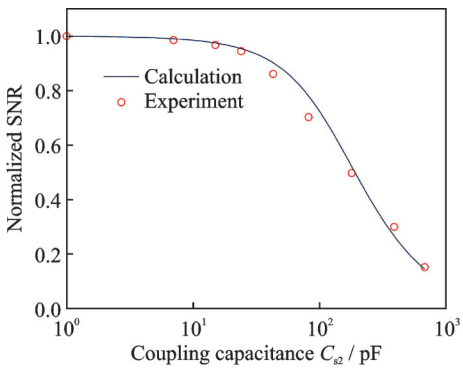

Fig.12 Relationship between SNR and C_{s2}

remain consistent with the theoretical curve. This scheme meets our energy expansion range requirements that expanding the energy range by 4—5 times for the first layer detector. A relative signal-to-noise ratio (SNR) plot combining output and noise data is shown in Fig.10. SNR is obtained by dividing the output from Eq.(3) by the noise from Eq.(6), then normalized to its maximum value. SNR drops to about one-quarter when the energy range is expanded fivefold, which is too low for low-energy particle detection. Therefore, a dual-channel readout system is proposed for the first-layer detector: One channel uses a small coupling capacitor for high-energy range, the other uses a normal coupling capacitor for high-precision detection.

Similarly, Figs.6,7 and Figs.8,9 show the relationships between the output signal amplitude and noise of the shaping network $V_{\text{out-shape}}$ and C_{s1} (C_{s2}). Output amplitude decreases with C_{s1} (C_{s2}), while noise increases. The experimental results are consistent with the theoretical analysis.

SNR is also critical for a particle detection system. Similarly, Figs.11 and 12 show SNR versus C_{s1} and C_{s2}, respectively, with other parameters fixed. The experimental results are consistent with the theoretical analysis. As shown, the SNR decreases with C_{s1} and C_{s2}, but the curves of the change are different. Thus, under low coupling capacitance, the influence of stray capacitance depends on whether C_{s1} dominates(Which means coupling capacitor is placed near the amplifier, and the value of C_{s1} is nearly equal to total stray capacitance) or C_{s2} dominates. For a small detector capacitance (e.g., C_x = 15 pF, C_d = 10 pF), SNR is higher when C_{s2} dominates. In our experiment, when C_{s2} is dominant SNR is 43.57, which is higher than SNR when C_{s1} is dominant (36.24) under the condition that total stray capacitance is nearly 9 pF. However, when the detector capacitance is large, the result is contrary that SNR when C_{s1} is dominant is larger (not shown here). This insight can guide printed circuit board (PCB) layout to optimize SNR when a long wire between detector and CSA is unavoidable.

Figs.4—12 present the output, noise, and SNR as a function of coupling capacitance and stray capacitance, respectively, with all results normalized to their max values. However, some individual data points deviate from theoretical values (e.g., the 390 pF data point in Fig.5), while some figures show that trends differ a little from theoretical results (e.g., Figs.4 and 6). Deviation of an individual data point is likely due to random experimental errors. The frequent manual swapping of capacitors during experiments may have caused slight inconsistencies in the circuit's ground state over time. The difference for high and low capacitances in Figs.4 and 6 can be attributed to the tolerance of capacitors and the stray capacitance induced by wiring(Though we have done our best to minimize stray capacitance). These impacts are more pronounced on low capacitance, leading to higher relative errors for small capacitance and likely account for the difference between high capacitance and low capacitance experimental results in Figs.4 and 6.

In summary, experimental results validate the theoretical model, which can guide component selection to expand energy range while maintaining acceptable SNR. Secondly, experiments show that we can expand the range up to 5 times, which meets the requirements for the first layer detectors, and the low SNR motivates us to design a dual-channel readout system for the first layer detector. Finally, under low coupling capacitance, stray capacitance at different positions has significant distinct effects on SNR. Since our instrument's detectors range from tens to hundreds of picofarads, coupling capacitor placement on the PCB can be optimized for higher SNR (e.g., placing it near the ASIC for the first-layer thin, large-capacitance detector).

3 Application Extension on RENA-3 System

This section demonstrates that the model is applicable to the RENA-3 readout system, confirming the feasibility of the energy-range expansion scheme. Additionally, certain RENA-3 parameters are extracted by fitting experimental data. These parameters are useful for our future application with RENA-3 chip.

Fig.13 shows the block diagram of RENA-3 experiments. Equivalent output charge method is also used to simulate the process of particles entering the detector and generating charges. In the experiment, RENA-3 serves as the ASIC. A field programmable gate array (FPGA) device is used to control the RENA-3 and AD9240 circuits to complete data collection. The values of C_{s1} and C_{s2} depend on the wiring layout. In the experiment, external parallel capacitors emulate different stray capacitance as shown in Fig.1.

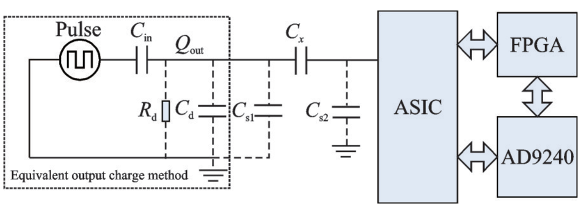

Fig.13 Block diagram of RENA-3 experiments

Direct verification of Eqs.(3, 5) is difficult because some RENA-3 parameters are unknown. However, the model's applicability can be assessed by fitting the output and noise curves. Unknown parameters are treated as fitting variables. For example, the terms $\frac{\tau A_0^2}{C_f^2}\left(\frac{kT}{2R_b}+\frac{kT}{2R_f}+\frac{qi_d}{4}+\frac{qi_g}{4}\right)$ and $\left(\frac{K_f A_0^2}{2C_g}+\frac{kTA_0^2}{3\tau g_m}+\frac{kTA_0^2}{2\tau R_d g_m^2}\right)$ will be set as fitting parameters respectively in Eq.(5). These parameters may vary slightly with experimental setup but should remain approximately constant within a given experiment set. For instance, leakage current may increase slightly when adding a parallel capacitor to emulate C_{s2}, but remains unchanged across experiments changing C_{s2}. In the previous experimental validation section, most parameters are known, allowing direct calculation. Here, fitting is used to test the model's applicability to RENA-3. One of the known parameters that influence curve shape is also included as a fitting variable to statistically validate the results. For example, if we change C_x, C_d will be set as a fitting parameter. The model is considered valid if: (1) the fitted curve matches the experimental trend, and (2) the fitted value of the known parameter agrees with its measured value.

Firstly, only the value of C_x is changed from 3.3 pF to 5 600 pF to get the relationship of normalized output signal amplitude and noise with the coupling capacitance, as shown in Fig.14. The data points marked by "." are experimental results and the solid line is fitting results, and this is similar for Fig.14 to Fig.16. In the experiments, no extra stray capacitance is added. The figures show that the fitting curve is consistent with the experimental results. C_d is used as a fitting parameter because it significantly affects the curve trend (according to Eqs. (3, 5)). The fitting value of C_d is (45±3.7) pF in Fig.14(a) and (37.4±8.9) pF in Fig.14(b), compared with the measured value of (44±0.5) pF.

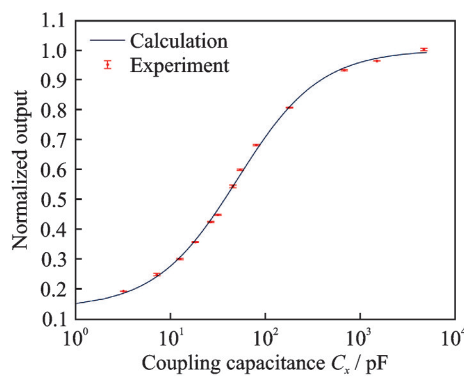

(a) Normalized output signal amplitude with the coupling capacitance

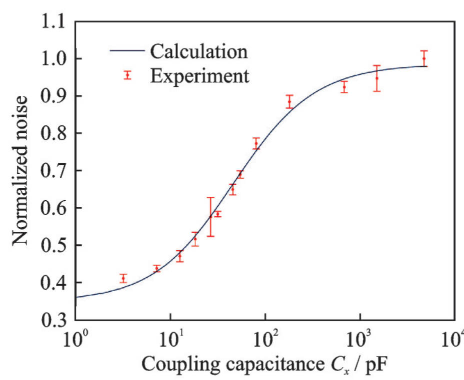

(b) Normalized noise with the coupling capacitance

Fig.14 Relationships between the normalized output signal amplitude and noise with the coupling capacitance

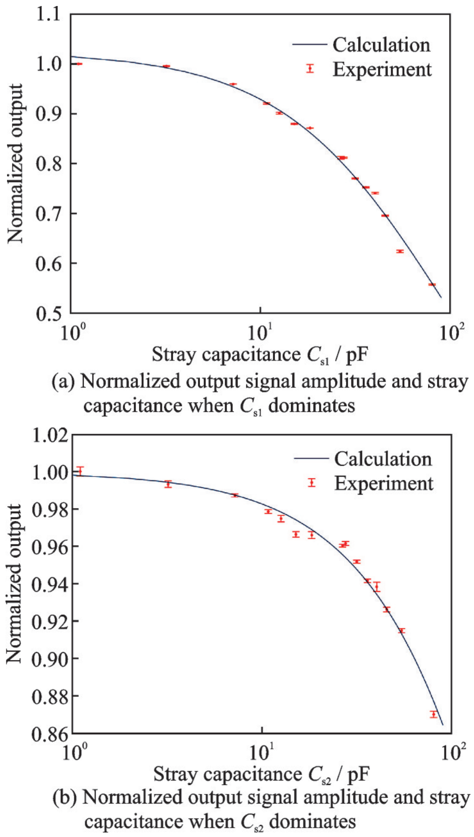

(a) Normalized output signal amplitude and stray capacitance when C_{s1} dominates

(b) Normalized output signal amplitude and stray capacitance when C_{s2} dominates

Fig.15 Relationships between the normalized output signal amplitude and the stray capacitance when C_{s1} or C_{s2} dominates

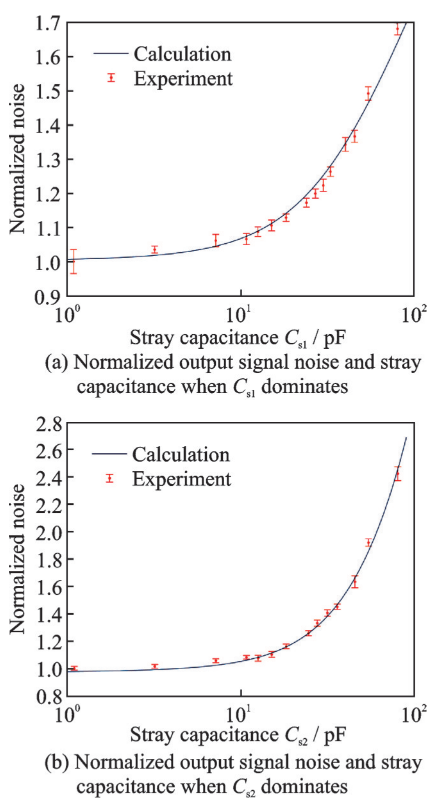

(a) Normalized output signal noise and stray capacitance when C_{s1} dominates

(b) Normalized output signal noise and stray capacitance when C_{s2} dominates

Fig.16 Relationships between the normalized output signal noise and the stray capacitance when C_{s1} dominates or C_{s2} dominates

Secondly, only the values of C_{s1} or C_{s2} are changed from 1 pF to 81 pF to get the relationships of normalized output signal amplitude and noise with the stray capacitors, as shown in Figs.15 and 16. The figures also show that the fitting curve is consistent with the experimental results. In Fig.15 (a), we set coupling capacitance C_x as fitting parameter (according to Eq.(3)). The fitting value of C_x is (95±5.6) pF in Fig.15(a) while the measurement value is (88±1) pF. In Fig.16(a), C_d is fitted as a major factor affecting noise besides stray capacitance (according to Eq.(5)). The fitting value of C_d is (1.9±1) pF in Fig.16(a), compared with the measured value of (1±0.1) pF.

The differences between the above mentioned experiment and the measured values may stem from component tolerances and unaccounted for noise sources (e.g., power-supply ripple). But within the error range, fitted values agree with measurements. Meanwhile, Fig.14(a) indicates that when $C_d \approx$ 44 pF, setting $C_x \approx 7$ pF extends the energy range by nearly a factor of four (≈9 MeV). This is sufficient for alpha-particle detection in the first-layer detector. The measuring error of C_d for a real detector will affect the final extended range and the estimation of SNR. If we set the error of C_d to 10% and use the parameters of the fitting in Fig.14, the error on the energy range and SNR could be calculated, which are both about 10%. Therefore, when expanding the energy range, a certain margin needs to be reserved. These experiments confirm the model's applicability to the RENA-3 readout system. Therefore, the experiment conclusion in section "Experiment Validation" can also be applied to RENA-3 readout system.

Finally, fitting also yields estimates of unknown RENA-3 parameters. In Fig.15(b), $(A+1)C_f$ is a major factor to affect output signal amplitude here (according to Eq.(3)). However, we cannot find a specific value of A in RENA-3 chip's manual. We can only provide the fitting result that $(A+1)C_f = (573\pm38)$ pF. The C_f used here is 60 fF, so the gain of RENA-3 chip is nearly 10^4 when the R_f is 200 MΩ and C_f is 60 fF. In Fig.16 (b), we set $C_d + C_g$ as a fitting parameter. According to Eq.(3), it is the major factor for noise besides stray capacitance. RENA-3 official manual only states $C_g \leqslant 5$ pF. The fitting value of $C_d + C_g$ is (5.3 ± 0.8) pF in Fig.16(b). According to the measurement value $C_d = (1 \pm 0.1)$ pF, we get that C_g of RENA-3 is (4.3 ± 0.8) pF. Considering the error range, the fitting value agrees with the manual. Table 2 lists these two extracted parameters not provided in the manual. These parameters could be useful in our future circuit design and PCB layout with RENA-3 circuit such as output and noise estimation in other circuit. And for each experiment above, the fitting results of unknown parameters we mentioned in this section are within an error of 20% except the C_d in Fig.16(a). However, the absolute error for C_d is only 1 pF. The percentage error is large due to the small nominal value.

Table 2 Fitting result of ASIC parameters

Parameter	Value
Open-loop gain A	$\approx 10^4$
Input capacitance C_g/pF	≈ 4.3

In this section, we validate that the model can be applied to RENA-3 by fitting the output and noise curves. Fitted values are close to actual component values, and curves match experimental trends. The deviations of individual data points in this section are consistent with those discussed in the "Experiment Validation" section. The open-loop gain and input capacitance are also extracted. Thus, the model is applicable to the RENA-3 readout system, and conclusions from the "Experiments Validation" section hold for RENA-3.

4 Conclusions

To extend the energy range for proton and ion channels of the RENA-3 chip in the IEPS instrument using small coupling capacitance, this paper presents a circuit theoretical model that calculates the transfer function from input charge to output voltage, analyzing the influence of coupling and stray capacitances. Experiments, using discrete devices with known parameters, are also done to verify the theoretical model. The model is then applied to the RENA-3 system for optimization, and certain RENA-3 parameters are obtained. The theoretical model provides an important reference for the circuit design and PCB layout for our instrument or other future application with RENA-3. It helps position the coupling capacitor to optimize SNR by managing the stray capacitance distribution.

Additionally, the experiments lead to a dual-channel readout system design. Two parallel coupling capacitors will connect to RENA-3, respectively. The value of one coupling capacitor is large such as 0.01—0.1 μF, and the other is as small as what we set in our experiment in this paper (such as 20 pF). Thus, for the same input, this produces two electronic signals: A large one and a small one. The large signal has high resolution but a lower upper energy limit, whereas the small signal has lower resolution but a higher upper energy limit. When the large-signal channel is not saturated, its output is used. For large input charges that saturate the large-signal channel, the small-signal channel, which continues to respond, is used. This expands the detectable energy range while preserving relatively low noise at low energies. However, crosstalk between channels may slightly increase low-energy noise compared with a single-channel system. We will conduct further exploration and research on this topic later.

Ultimately, the energy range can be extended to approximately 9 MeV, about four times the experimental linear range or eight times the official manual specification. This kind of design can solve the problem that RENA-3 cannot meet the requirement for energy range of proton and ion channels for our instrument.

References

[1] SAFAVI-NAEINI M, FRANKLIN D R, LERCH M L F, et al. Evaluation of silicon detectors with integrated JFET for biomedical applications[J]. IEEE Transactions on Nuclear Science, 2009, 56(3): 1051-1055.

[2] SAMPIETRO M, FASOLI L, BERTUCCIO G. Source follower or charge amplifier? An experimental comparison using a detector with integrated electronics[J]. IEEE Transactions on Nuclear Science, 1996, 43(4): 2413-2418.

[3] GIACOMINI G, BOSISIO L, DALLA BETTA G F, et al. Integrated source follower for the read-out of silicon sensor arrays[J]. IEEE Transactions on Nuclear Science, 2015, 62(5): 2187-2193.

[4] DALLA BETTA G F, PIGNATEL G U, VERZELLESI G, et al. Monolithic integration of Si-PIN diodes and n-channel double-gate JFET's for room temperature X-ray spectroscopy[J]. Nuclear Instruments and Methods in Physics Research Section A: Accelerators, Spectrometers, Detectors and Associated Equipment, 2001, 458(1/2): 275-280.

[5] GRYBOS P, KACHEL M, KMON P, et al. Low noise 64-channel ASIC for AC and DC coupled strip detectors[J]. IEEE Transactions on Nuclear Science, 2011, 58(1): 187-193.

[6] ZHAI Qingtai. Development of a novel delta EE particle identification telescope readout system[D]. Boston: Boston University, 2007.

[7] DALLA BETTA G F, PIGNATEL G U, VERZELLESI G, et al. Si-PIN X-ray detector technology[J]. Nuclear Instruments and Methods in Physics Research Section A: Accelerators, Spectrometers, Detectors and Associated Equipment, 1997, 395(3): 344-348.

[8] KNOLL G F L. Radiation detection and measurement [M]. 4th ed. Hoboken NJ: Wiley, 2010.

[9] TSOULFANIDIS N, LANDSBERGER S. Measurement & detection of radiation[M]. 5th ed. Boca Raton: CRC Press, 2021.

[10] SUN Zezhou, MENG Linzhi. Current situation and sustainable development trend of deep space exploration in China[J]. Journal of Nanjing University of Aeronautics & Astronautics, 2015, 47(6): 785-791. (in Chinese)

[11] YU Xiangqian, WANG Linghua, WANG Yongfu, et al. Design of an interplanetary ultralow-noise three-dimensional energetic particle spectrometer[J]. Reviews of Geophysics and Planetary Physics, 2024, 55(3): 308-316. (in Chinese)

[12] TUMER T O, CAJIPE V B, CLAJUS M, et al. Multi-channel front-end readout IC for position sensitive solid-state detectors[C]//Proceedings of 2006 IEEE Nuclear Science Symposium Conference Record. San Diego, CA, USA: IEEE, 2007: 384-388.

[13] ZOU H, YE Y G, ZONG Q G, et al. Imaging energetic electron spectrometer onboard a Chinese navigation satellite in the inclined GEO orbit[J]. Science China Technological Sciences, 2018, 61(12): 1845-1865.

[14] YE Y G, LI J W, HUANG C, et al. Medium-energy electron detector onboard the FY-3E satellite[J]. Space Weather, 2023, 21(3): e2022SW003241.

[15] YE Y G, ZOU H, ZONG Q G, et al. Energetic electron detection packages on board Chinese navigation satellites in MEO[J]. Earth and Planetary Physics, 2021, 5(2): eepp2021021.

[16] YE Y G, LIU Y, ZOU H, et al. Medium-energy electron spectrometers on Macao science satellite-1[J]. Science China Technological Sciences, 2024, 67 (11): 3324-3343.

Acknowledgements This work was supported in part by the National Natural Science Foundation of China under contracts (Nos. 42127803, 42225404, 42150105) and the National Key R&D Program of China (No.2023YFC2808904).

Authors

The first author Mr. **YANG Xin** received the B.S. degree from the Institute of Space Physics and Applied Technology at School of Earth and Space Sciences, Peking University, Beijing,China in 2021. He is currently pursuing his Ph.D. degree at the Institute of Space Physics and Applied Technology at School of Earth and Space Sciences, Peking University. His research interests include physical design, physical simulation and experiment for interplanetary energetic particle Spectrometer.

The corresponding author Prof. **WANG Linghua**, the project leader for IEPS, studied under the renowned space physicist and space exploration instrument developer, Robert Lin, from the University of California, Berkeley. She has been dedicated to researching the origin, acceleration, and transport processes of interplanetary energetic particles. She has participated in the development and observational analysis of particle detectors for multiple international space exploration projects, such as WIND, STEREO, CINEMA, and Solar Orbiter. She has been in charge of the calibration and interpretation of the detection data from the WIND/3DP and STEREO/STE instruments and serves as a Co-Investigator for the EPD instrument on the Solar Orbiter and the MPPE instrument on the BepiColombo MMO.

Author contributions Mr. **YANG Xin** completed the experiment, organized the data, drew conclusions, and wrote the original manuscript. Dr. **YU Xiangqian** provided the idea and reviewed the result. Prof. **WANG Linghua** is principal investigator of the IEPS instruments. Mr. **WANG Youlong** wrote the main code of FPGA (control of RENA-3). All authors commented on the manuscript draft and approved the submission.

Competing interests The authors declare no competing interests.

(Production Editor: XU Chengting)

基于RENA-3的粒子探测系统中低耦合电容影响研究

杨　芯[1,2]，王玲华[1,2]，于向前[1,2]，施伟红[1]，陈鸿飞[1]，王游龙[1]，王永福[1]，宗秋刚[1]，邹　鸿[1]，叶雨光[1]

（1.北京大学地球与空间科学学院空间物理与应用技术研究所，北京100871，中国；2.中国科学院国家空间科学中心太阳活动与空间天气国家重点实验室，北京100190，中国）

摘要：粒子探测系统的性能主要由其第一级放大电路决定，主要包括粒子辐射探测器和电荷灵敏放大器(Charge-sensitive preamplifier, CSA)。探测器与前端读出电路之间的连接通常采用交流耦合方式，配备一个在0.01～0.1 μF的范围内的耦合电容，将CSA的输入与探测器隔离开来。专用集成电路(Application-specific integrated circuit, ASIC)RENA-3是一种多通道混合信号集成电路(Integrated circuit, IC)，具有高能量分辨率和高时间分辨率的特点，专为粒子辐射探测器的读出电路而设计。行星际超低噪声三维能量粒子谱仪被设计为利用RENA-3作为前端电路，探测20～1 000 keV电子、25～12 000 keV质子和α粒子这样的离子。然而，RENA-3的最大输入电荷为54 fC，这限制了它的最大探测范围约为1 200 keV，这个能量不足以满足仪器质子探测的能量范围需求。虽然也可以采用其他ASIC，但现有的替代方案无法同时满足高精度和宽测量范围的要求。本文提出采用一个小的耦合电容，在电荷信号到达CSA输入之前对其进行衰减，来扩展ASIC的探测范围。该耦合电容的大小在皮法量级，需要小于探测器结电容。在这种配置下，杂散电容和耦合电容对电路性能的影响变得非常重要。本文提出了一种电路理论模型来计算从输入电荷到输出电压的传递函数，分析了耦合电容和杂散电容对粒子辐射检测系统的影响。使用已知参数的分立元件进行实验来验证理论模型。然后将该模型应用于RENA-3系统并按照仪器指标进行相应电路优化。实验结果显示，通过减小耦合电容的方法能够将RENE-3的能量探测范围至少扩大到9 MeV，这个能量满足仪器的质子探测指标。最后，杂散电容对小耦合电容的读出电路影响较大，本文分析了不同杂散电容对电路的影响，认为不同电容大小的探测器应采取不一样的电路板布局，能够通过改变杂散电容的分布从而得到更高的信噪比。

关键词：交流耦合电路；耦合电容；杂散电容；电路表现；粒子辐射探测系统

研究亮点：

1. 提出了一种电路理论模型来计算从输入电荷到输出电压的传递函数。
2. 成功实现将RENA-3的能量探测范围至少扩大到9 MeV，并应用于行星际超低噪声三维能量粒子谱仪。
3. 探究在小耦合电容条件下，不同杂散电容对电路的影响，提出根据不同探测器电容改变杂散电容分布从而获得更高的信噪比。
4. 实验中通过分析得到RENA-3部分关键参数。